1

Property Tailoring of Gold Clusters via Surface Engineering and Supramolecular Assembly

1.1 Introduction

Monolayer-protected gold nanoclusters (NCs), with sizes in between simple complexes and nanoparticles, are a class of newly emerging materials that possess discrete energy levels and show intriguing photophysical and catalytic properties that benefit from the quantum confinement effect [1–3]. The well-defined structures reveal that such gold NCs usually adopt core–shell configuration. The ligand shell is found to have a significant impact on the geometrical structures, electronic structures, and properties of metal NCs except for their most primitive role in preventing aggregation [4]. Developing strategies to rationally modify the surface of the gold clusters, with the metal core maintained, is of great importance to achieve functionalized metal nanomaterials and to reveal the surface impact on the properties of gold clusters.

What is more, beyond molecules, the condensed state of gold NCs, which is known as gold cluster-assembled materials (GCAM), supported by intermolecular interactions, is also attractive with new collective properties [5, 6]. For instance, intercluster aggregations induced by the addition of poor solvents, or cations to the solution of metal NCs, may display enhanced PL intensities – a phenomenon known as aggregation-induced emission (AIE) [7, 8]. As a common aggregated form, the solid-state metal cluster-assembled materials show promising applications in many fields (e.g. fluorescence, catalysis, chirality, magnetism, electrochemistry, etc.) [9], and their properties highly depend upon the packing modes and the intercluster interactions. The self-assembly of NCs is usually driven by hydrogen bonding, electrostatic interactions, van der Waals interactions (including dipolar, C–H···π, and π···π interactions), facilitated by the surface ligands between neighboring NCs, and, in some cases, the metallophilic and amphiphilic interactions [5, 6, 9, 10]. In recent years, the externally directed assembly of NCs by adding external reagents such as metal ions and bridging ligands has been explored [4].

In this chapter, we discuss the surface engineering and hierarchical assembly strategies usually employed to endow gold NCs with customized functionalities.

Atomically Precise Metal Clusters: Surface Engineering and Hierarchical Assembly,
First Edition. Shuang-Quan Zang.

Given the limitation of space, only gold NCs with atom-precise structure and composition are summarized here. The potential applications of GCAMs in fields, including semiconductivity, magnetism, and biomedicine, are also introduced with attractive representatives.

1.2 Surface Modification of Gold NCs

The ligand shell of monolayer-protected gold NCs determines their solubility, stability, and reactivity; thus, modification of the out shell may dramatically impact the inherent properties and enable functionalization of gold NCs for their use in bioimaging, catalysis, theranostics, and sensing applications. In this section, we introduce several well-developed strategies, including ligand exchange, post-modification, and surface locking by metals, for metal core-maintained surface modification of gold NCs.

1.2.1 Ligand Exchange

In nanoscience, ligand exchange is a highly versatile strategy for the functionalization and tailoring of the surface properties of nanoparticles. In many cases, the ligand exchange would lead to size or structure transformation because of the high reactivity between metal NCs and the incoming ligands, the different binding modes of the ligands to metal atoms, and the poor stability of the target NC required to maintain the metal core structures. Thus, ligand exchange-induced size/structure transformation (LEIST) has become a new methodology to expand the "library" of monolayer-protected metal NCs for the exploration of their magic sizes, structures, properties, and applications [11]. In this section, we focus only on the metal core-maintained examples of ligand exchange through the types of incoming ligands, which usually take place with ultrastable metal NCs such as Au_8, Au_{13}, Au_{25}, Au_{38}, and Au_{102}.

1.2.1.1 Thiolate/Selenolate as Incoming Ligands

With respect to atomically precise NCs, thiolate ligand exchange process has been applied to introduce functionality to the NCs' exterior ligand shell. Murray and coworkers performed extensive work on ligand exchange on $Au_{25}(PET)_{18}$ with various SR (where PET = SCH_2CH_2Ph, R = Ph-CH_3, Ph-F, etc.), and this Au_{25} NC can accommodate many different types of thiolate ligands, as evidenced in the observation of the $Au_{25}(SR)_{18-x}(SR')_x$ series (where x can be up to 12) [12–14]. Pradeep and coworkers also performed ligand exchange on $Au_{25}(SG)_{18}$ with functionalized glutathione, with the purpose of tuning the optical properties of the $Au_{25}(SR)_{18}$ [15]. Furthermore, selenolate for thiolate exchange was also reported in the $Au_{25}(SR)_{18}$ case by Negishi and Zhu groups, and the stability of the resultant $Au_{25}(SeR)_{18}$ was found to be enhanced [16, 17]. Zhong et al. investigated the energetics of ligand exchange of thiolate-protected Au NCs with selenol and revealed that the formation of selenolate-protected Au NCs is thermodynamically favorable from ligand exchange reaction [18]. In regard to the

characterization of mixed-ligand shell NC, Negishi and coworkers successfully achieved the isolation of each component of the mixed-ligand $PdAu_{24}(SR)_{18-x}(SR')_x$ and $Au_{25}(SR)_{18-x}(SR')_x$ series using HPLC [19]. And the mixed-thiolate ligand shell has also been observed by X-ray crystallography.

Heinecke et al. reported the partial ligand exchange of parabromobenzenethiol (*p*-BBT) onto the $Au_{102}(p\text{-MBA})_{44}$ NC (*p*-MBA = para-mecaptobenzoic acid) [20]. When the feed ratio of *p*-BBT to the *p*-MBA on the cluster was kept at 2 : 44, partially exchanged $Au_{102}(p\text{-MBA})_{40}(p\text{-BBT})_4$ resulted in very fast kinetics (e.g. in five minutes). The x-ray crystal structure shows that the exchanged thiolate positions were on the two poles of the fivefold symmetric dodecahedral kernel, which are the most accessible sites on the Au_{102} NC. A similar ligand exchange reaction was also performed on $Au_{25}(PET)_{18}$ by the same group, and the partially ligand exchanged product $Au_{25}(PET)_{16}(p\text{-BBT})_2$ was successfully crystallized [21]. It is worth noting that the mixed ligand shelled NCs could also be synthesized via direct reduction of gold salts in the presence of multiple types of ligands. For example, Yuan et al. reported a facile synthesis of mono-, bi-, and trithiolate-protected $Au_{25}(SR)_x(SR'')_y(SR''')_{18-x-y}$ NCs via a NaOH-mediated $NaBH_4$ reduction method [22]. Ligand exchange has also been extensively employed to introduce chirality into the gold NCs by using chiral thiolate ligands. Bürgi and coworkers reported the use of a chiral bidentate thiol, (R)-BINAS (note: BINAS = 1,1′-binaphthyl-2,2′-dithiol), to perform ligand exchange with the racemic $Au_{38}(PET)_{24}$ NCs at room temperature, with a ratio of BINAS : $Au_{38}(PET)_{24}$ = 120 : 1 or BINAS : PET = 5 : 1 [23]. It was found that two PET ligands on the Au_{38} were exchanged by one (R)-BINAS, and further exchange with a second (R)-BNAS ligand showed a much slower rate. They also found that the (R)-BINAS had a preference for the left-handed Au_{38} cluster, manifested in a ligand exchange rate four times higher compared to that for the right-handed Au_{38} cluster [24]. Lately, the same group investigated the electronic and stereospecific effects during LERs with achiral $Au_{25}(2\text{-PET})_{18}$ NCs, depending on the enantiopure BINAS ligand and the corresponding fluorine-substituted molecule. The results indicate that the stereospecific effect is a local property at the surface of the cluster, whereas the electronic effect due to the adsorbed ligand extends over the whole cluster and significantly influences the kinetics of further LERs. This work offers new insight for the design of new ligands and a strategy to control LERs [25]. Very recently, Suzuki et al. isolated a series of mono-ligand exchanged Au_{25} cluster anions ($[Au_{25}(SR)_{17}(SR')]^-$) by employing porphyrinthiol derivatives as a bulky incoming ligand (Figure 1.1). Through modification of the structures of the incoming porphyrin ligands, they revealed that the dominant factor in controlling the exchanged position of SR′ is the steric hindrance of an incoming ligand instead of the electronic effects. And the steric repulsion between the protecting ligands is also a critical factor for perturbing the core structure of the Au_{25} cluster anion as evidenced by the X-ray absorption fine structure (XAFS) analysis [26].

1.2.1.2 Alkynyl as Incoming Ligands

Synthesis of acetylide-protected metal clusters proceeds most often by the reduction of Au(I)-acetylide complexes [27]. Gold-alkynyl NCs prepared by post-synthetic

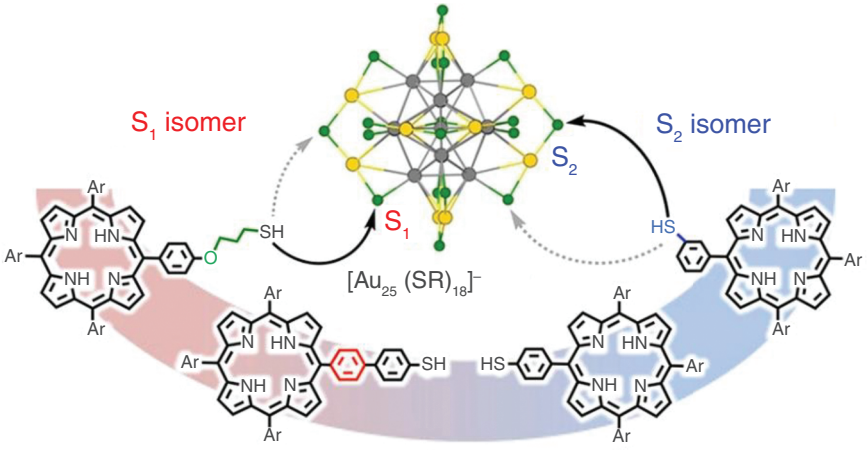

Figure 1.1 Control over regioselectivity by steric effect. Source: With permission from Ref. [26]. © 2022 American Chemical Society.

acetylide exchange with intact metal skeletons, particularly those with precise crystal structures, are very scarce.

The Konishi group achieved the regioselective introduction of two alkynyl ligands on the surface of the icosahedral Au_{13} skeleton by the ligand exchange reaction of a dichloro-substituted Au_{13} cluster cation $[Au_{13}(dppe)_5Cl_2]^{3+}$ [28]. The reaction cleanly proceeded by employing excess amounts of terminal alkynes and base (sodium methoxide), and the complete ligand exchange was verified by electrospray ionization mass spectrometry (ESI-MS) analysis of the reaction mixture. Crystal structural analysis reveals that two alkynyl ligands in the obtained $[Au_{13}(dppe)_5(C{\equiv}CPh)_2]^{3+}$ are σ-coordinated to the two diagonal apexes of the icosahedron from the *trans* positions (Figure 1.2). The σ-coordination of alkynyl ligands to the gold cluster surface is much different from the binding interface found in larger gold–alkynyl clusters

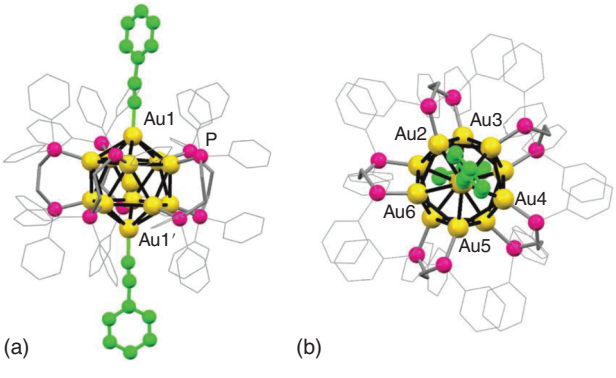

Figure 1.2 (a) Side and (b) top views of the crystal structure of the cationic moiety of $[Au_{13}(dppe)_5(C{\equiv}CPh)_2]^{3+}$. Phenylethynyl units (C≡CPh) are highlighted in light green, and the hydrogen atoms are omitted for clarity. Source: With permission from Ref. [28]. © 2015 The Royal Society of Chemistry.

synthesized by the reduction of gold(I) alkynyl precursors [27], indicating the uniqueness of the post-synthetic ligand exchange method. This work also demonstrated the presence of an electronic interaction of gold superatom with a σ-bonded π-system.

Notably, Hosier et al. revealed acetylide-for-thiolate and thiolate-for-acetylide exchanges on gold NCs for the first time [29]. They reported the success or failure of exchange with different acetylide derivatives and/or reaction conditions and concluded that forward exchange, reverse exchange, and interparticle ligand exchange are all facile reactions with suitable incoming ligands. With regard to acetylide-for-thiolate exchange, when phenylacetylene is introduced as a gold(I) or lithium phenylacetylide complex, exchange on thiolate-protected gold clusters is successful in mild conditions, whereas the reaction failed when employing free phenylacetylene under various conditions including ligand concentrations, temperatures, and the presence of an exogenous base.

1.2.1.3 N-Heterocyclic Carbenes (NHCs) as Incoming Ligands

Although diverse ligands including thiolate, alkynyl, phosphine have been employed to passivate the nanoscaled metal NCs and endow them with intriguing properties, the lack of other strongly bound ligands for NCs with different bonding modes has been a significant limitation in the field. In 2019, Narouz et al. first introduced N-heterocyclic carbenes (NHCs) to the phosphine-stabilized undecagold clusters by ligand exchange reaction, which feature a robust metal–carbon single bond and impart high stability to the corresponding gold cluster (Figure 1.3) [30]. Phosphine-stabilized clusters were chosen because NHC and phosphine ligands are both neutral and thus require no change in oxidation state or cluster charge to accompany an exchange reaction. The addition of a single NHC to gold NCs results in significantly improved stability and catalytic properties in the electrocatalytic reduction of CO_2. By varying the conditions, nature, and number of equivalents of the NHC, predominantly or exclusively

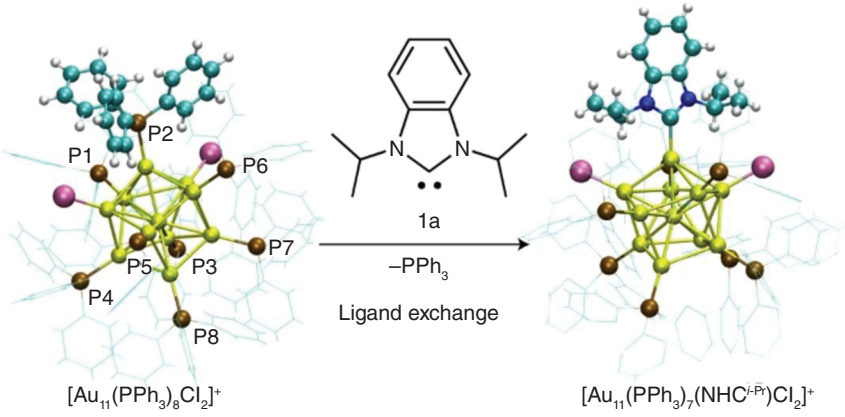

Figure 1.3 Illustration of the NHC-for-phosphine ligand exchange on $[Au_{11}(PPh_3)_8Cl_2]^+$. Source: With permission from Ref. [30]. © 2019 Springer Nature Limited.

monosubstituted NHC-functionalized clusters result. Clusters can also be obtained with up to five NHCs as a mixture of species. This work greatly encourages the investigation of NHCs as protecting ligands, and a number of NHC-stabilized metal clusters with atom-precise crystal structures have been reported since then [31–39].

1.2.2 Surface Locking Through Coordination

The molecular flexibility is the main reason for the nonradiative relaxation and usually causes the luminescence quenching. With respect to the monolayer-protected metal NCs, the surface rigidity significantly influences their emission behaviors. The novel hexaauriomethane $[(Ph_3PAu)_6C](BF_4)_2$, first reported by Schmidbaur and coworkers emits green light in the solid state upon irradiation with UV light but is not emissive in solution at room temperature [40]. The nonradiative relaxation is probably attributed to the rotation of the outer Ph_3P. To achieve the phosphorescence enhancement, it is necessary to close this nonradiative pathway by hindering the rotation of Au—P bonds. The Wang group reported a facile approach, that is, tying up the peripheral phoshines by introducing additional coordination, i.e. functionalizing $[(Ph_3PAu)_6C]^{2+}$ by using diphenylphoshpino-2-pyridine (dppy) in place of triphenylphosphine to form $[Au_6(C)(dppy)_6](BF_4)_2$, which is followed by installing a silver atom, and thus the rigidity of the cluster is increased (Figure 1.4). The resulting novel heteronuclear gold(I)–silver(I) cluster $[Au_6Ag_2(C)(dppy)_6](BF_4)_4$ is strongly emissive in solution at room temperature [41].

To achieve higher quantum yield (QY), it is desirable to fully protect the emissive core. To this end, the same group employed bis(2-pyridyl)phenylphosphine ($PPhpy_2$) as the peripheral ligand [42]. Unlike dppy, which has only one pyridyl group, there are two pyridyl groups in $PPhpy_2$, which offers one more coordinating donor for metal binding. More silver ions introduced into the cluster to limit the motion of the organic ligands may facilitate stronger luminophores. Using this strategy, they obtained the strong luminescent adducts $[(C)(AuPPhpy_2)_6Ag_4](BF_4)_6$ and $[(C)\text{-}(AuPPhpy_2)_6Ag_6(CF_3CO_2)_3](BF_4)_5$ by rationally adding silver salts (Figure 1.5). It is of special interest that the latter NC emits very intense yellow light with a QY of 92% in CH_2Cl_2/CH_3OH (1 : 1, v : v) at room temperature.

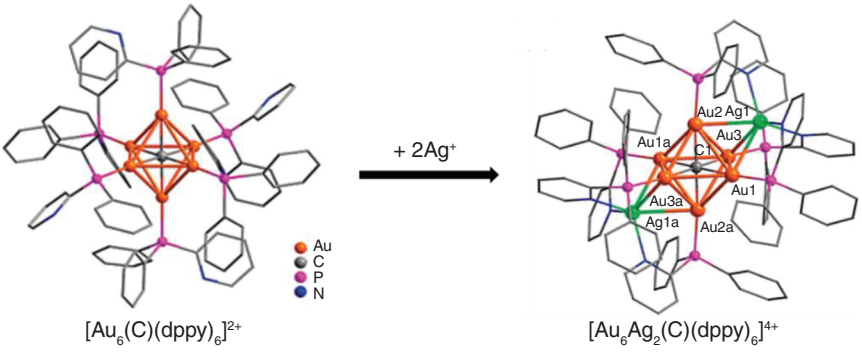

Figure 1.4 Illustration of the surface locking on $[Au_6(C)(dppy)_6]^{2+}$. Source: Reproduced with permission from Ref. [41]. © 2009 American Chemical Society.

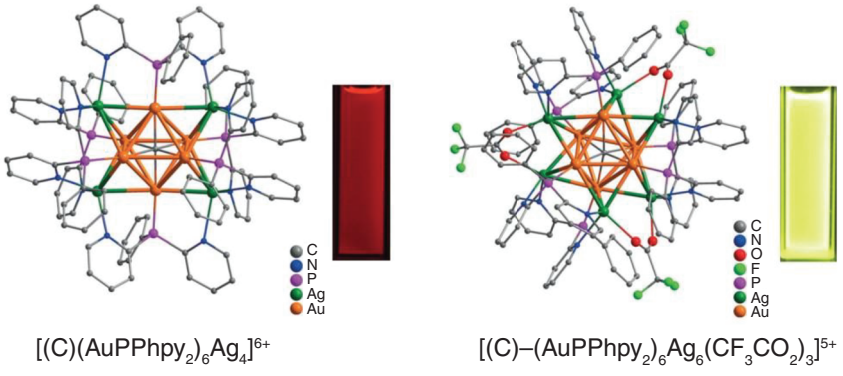

Figure 1.5 Structures and emission photos of $[(C)(AuPPhpy_2)_6Ag_4]^{6+}$ (left) and $[(C)\text{-}(AuPPhpy_2)_6Ag_6(CF_3CO_2)_3]^{5+}$ (right). Source: Reproduced from Ref. [42]. © 2017 John Wiley & Sons.

1.2.3 Post-Assembly Surface Modification

Surface chemical reactions on atomically precise metal clusters have received considerable attention for opening a new platform for cluster functionalization. Gunawardene et al. reported the direct synthesis of a surface-reactive gold NC platform, which utilizes an azide-functionalized thiol ligand ($HSCH_2CH_2$-*p*-C_6H_4-N_3) to give a surface-reactive $[(CH_3\text{-}(CH_2)_7)_4N]\text{-}[Au_{25}(SCH_2CH_2\text{-}p\text{-}C_6H_4\text{-}N_3)_{18}]$ (1-azido) [43]. To establish simple proof of concept cluster-surface strain-promoted alkyne-azide cycloaddition (CS-SPAAC) reactivity of the platform, they reacted 1-azido with a symmetrical strained-cyclooctyne, which greatly aided the characterization of the modified platform. The results showed that all surface azide moieties are available for CSSPAAC while retaining the internal NC core configuration (Figure 1.6). Such post-assembly CS-SPAAC on the azide-functionalized $[Au_{25}(SR)_{18}]$ platform provides an exciting new avenue toward the development of structurally and multifunctionally complex $[Au_{25}(SR)_{18}]$ NCs, whose molecular-type physical and chemical properties can more easily be tuned for potential applications.

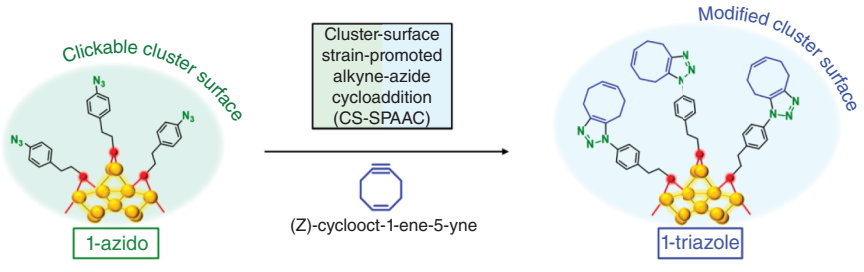

Figure 1.6 CS-SPAAC reaction between $[(CH_3\text{-}(CH_2)_7)_4N][Au_{25}(SCH_2CH_2\text{-}p\text{-}C_6H_4\text{-}N_3)_{18}]$ (1-azido) and (Z)-Cyclooct-1-ene-5-yne, giving surface-modified $[(CH_3\text{-}(CH_2)_7)_4N][Au_{25}(SCH_2CH_2\text{-}p\text{-}C_6H_4\text{-}C_8H_{10}N_3)_{18}]$ (1-triazole). Source: From Ref. [43]. © 2019 American Chemical Society.

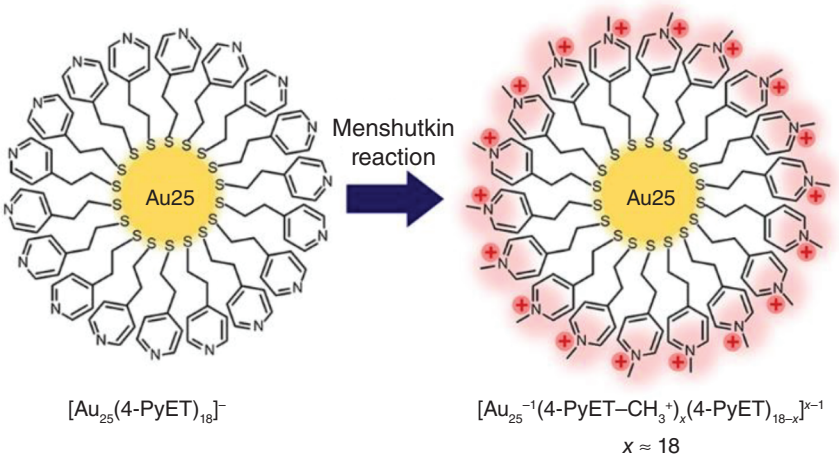

Figure 1.7 Menshutkin (methylation) reaction on $Au_{25}(4\text{-PyET})_{18}$ clusters. Source: With permission from Ref. [44]. © 2021 American Chemical Society.

The Menshutkin S_N2 reaction is a common method to obtain the quaternary ammonium salt ($[-N(CH_3)_3]^+$) by reacting a tertiary amine with an alkylating agent. The Yonezawa group demonstrated the Menshutkin (methylation) reaction of the surface pyridyl (py) moieties on basic $Au_{25}(4\text{-PyET})_{18}$ clusters (4-PyET = $-SCH_2CH_2Py$) for their successful transformation into cationized $Au_{25}(4\text{-PyET-}CH_3^+)_x(4\text{-PyET})_{18\text{-}x}$ clusters without altering their Au_{25} cores (Figure 1.7) [44]. By changing the methylating reagent, reaction time, and number of reaction cycles, they succeeded in controlling the number of methylated ligands (x); an x of approximately 18 (i.e. fully methylated $Au_{25}(4\text{-PyET-}CH_3^+)_{18}$) was obtained under the optimal condition. This work provides a novel idea for diversifying the R-groups of molecular metal clusters through the surface chemical reaction.

1.3 Gold Cluster-Assembled Materials (GCAMs)

Considerable interests in coordinated metal clusters in condensed states, namely "GCAM," have recently developed [45]. Such condensed situations are expected to cause synergetic effects among multiple cluster molecules, which may lead to the emergence of unique properties that are not found in single clusters. By using coordinated clusters with unique intrinsic properties and electronic structures such as the zero-dimensional precursory components, one can envision the strategical atomic-level design of cluster-based functional materials through controlled assembling or chemical transformations (Figure 1.8). In this section, we only focus on the GCAMs based on atom-precise gold clusters linked by metal–metal bonds and covalent bonds.

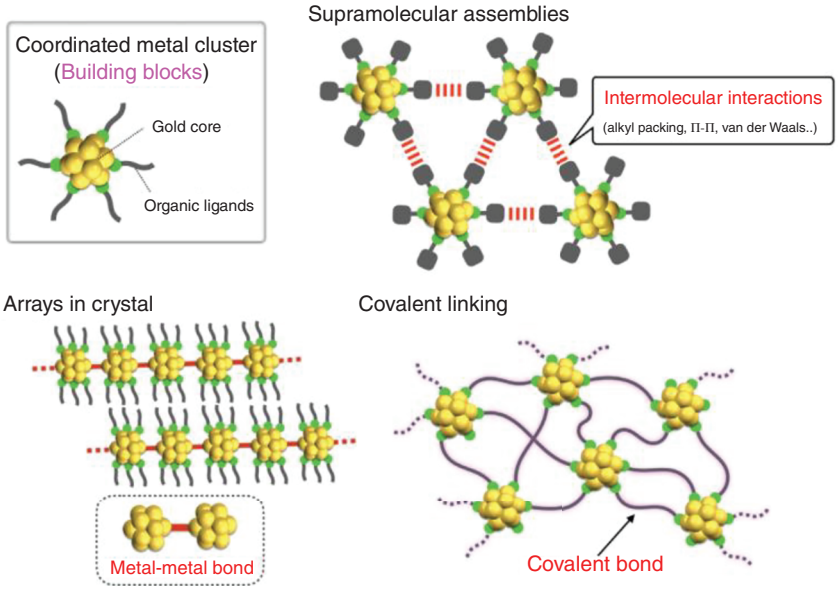

Figure 1.8 Schematic illustration of several forms of coordinated metal clusters in the condensed states. Source: With permission from Ref. [45]. © 2022 Elsevier.

1.3.1 1D Cluster Arrays Bridged by Metal–Metal Bonds

In 2014, Maran and coworkers reported the structure of a neutral $[Au_{25}(SBu)_{18}]^0$ cluster (SBu = 1-butanethiolate), showing a unique 1D array in which Au_{25} clusters are connected via Au—Au bonds (Figure 1.9a) [46]. They mentioned that BT would be the optimal length to induce intercluster Au—Au bond formation because it is not so bulky and allows facile interdigitation between the ligands. The involvement of the interactions mediated by the C4 segments is supported by the comparison of

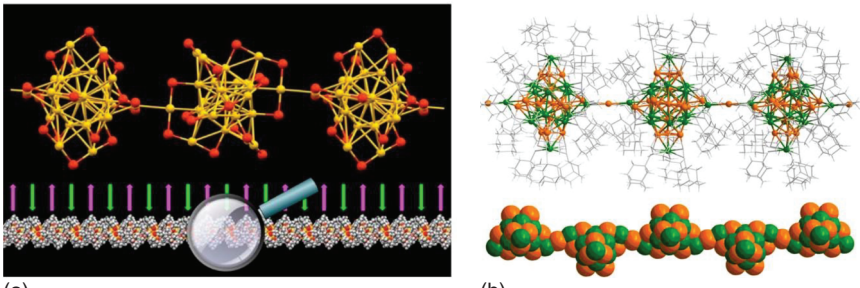

Figure 1.9 (a) Stick-and-ball view of the $Au_{25}(S)_{18}$ skeletons in the $Au_{25}(SBu)_{18}$ crystal. Au = yellow, S = red (in the first three panels, C and H atoms are removed for clarity). Source: With permission from Ref. [46] (2014)/American Chemistry Society. (b) Atomic structure of the polymer based on $(AuAg)_{34}$ clusters. Colors: golden and green, Au/Ag; gray C. All hydrogen atoms are omitted for clarity. Source: With permission from Ref. [47]. © 2020 Springer Nature Limited.

the crystal packing feature of $[Au_{25}(SEt)_{18}]^0$ with less bulky thiolate (SEt = ethanethiolate), whose cluster components are not connected via Au—Au bond and are molecularly isolated from each other. The unique linear orientation of $[Au_{25}(SBu)_{18}]^0$ cluster in the crystalline state is likely associated with the absence of counterions, which may enable dense packing of clusters. They also developed a simple large-scale method based on electro-crystallization for the preparation of the linear arrays of $[Au_{25}]^0$ from anionic $[Au_{25}]^-$ cluster [48].

Recently, Zheng and coworkers reported an example of the linear arrangement of 1-ethynyladamantane-protected $(AuAg)_{34}$ clusters, in which each pair of the clusters is bridged by one gold atom (Figure 1.9b) [47]. In the synthesis of the 1D cluster polymer, they found that the use of CH_2Cl_2 as the solvent for crystallization results in the formation of a linear array of $(AuAg)_{34}$ clusters. On the other hand, the $(AuAg)_{34}$ monomer was isolated in crystals when CH_2Cl_2 was replaced with $CHCl_3$, indicating that the formation of the 1D array involves solvent-mediated processes.

1.3.2 Covalently Bridged Oligomers and Networks

Bridging between two or more metal clusters using multidentate ligands has been attempted in order to obtain insights into the interplay between two or more metal cores, which may give rise to unusual optical and electronic properties and bifunctional catalytic effects. The ligand exchange method using bidentate ligands offers a straightforward approach, but it is not easy to elucidate the reaction pathway and mechanism. Also, their complicated dynamic equilibrium must be considered. Lahtinen and coworkers tackled this subject through both simulation and experiments [49]. They used a monodisperse $Au_{\sim 250}(p\text{-MBA})_n$ cluster as the starting material and examined the oligomerization through the ligand exchange using five types of aryl dithiols as linkers.

For the separation of oligomers, polyacrylamide gel electrophoresis (PAGE) was applied. Dimer, trimer, and tetramer of $Au_{\sim 250}$ clusters were successfully isolated, which were characterized by the TEM measurements. They further analyzed the relation between ligand-to-cluster ratio and the yields of oligomers from simulations and showed that the yields strongly depend on the molar amount of the dithiol rather than the length/structure of the dithiol spacers. In addition, it was shown that the isolated oligomer fractions immediately began to re-equilibrate to afford new oligomer sets once they were dissolved in solution. These results provide important implications that the reversibility of the thiol exchange must be considered to assess the stabilities and properties of isolated cluster oligomers.

The ligand exchange reactions of $Au_{25}(SR)_{18}$-type clusters with various alkanedithiols have been also investigated. Dass and coworkers reported the exchange reaction of $[Au_{25}(PET)_{18}]^-$ and a series of linear alkanedithiols, showing that intramolecular crosslinking concomitantly occurs when the length of the alkyl spacer is short [50]. Aromatic *p*-conjugate systems have been also employed as the linkers to investigate the possibility of mediated electron coupling between two or several coordinated gold clusters. Bürgi and coworkers attempted the bridging of $[Au_{25}(SR)_{18}]^0$ clusters using rigid conjugated aromatic dithiols (Figure 1.10) [51]. Through the ligand

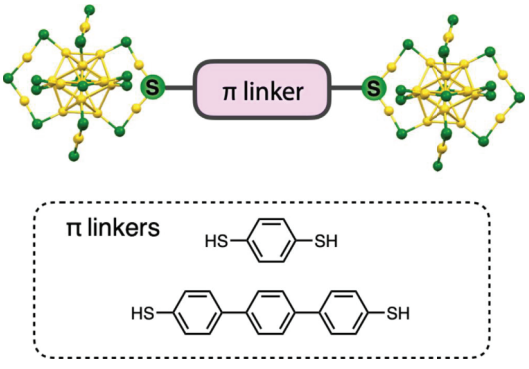

Figure 1.10 Au_{25} dimer bridged by an aromatic linker. Source: With permission from Ref. [45]. © 2022 Elsevier.

exchange reaction between monomeric 1-butanethiolate-modified Au_{25} cluster and dithiols, they obtained several Au_{25} oligomers after the purification using SEC. The absorption spectra of the separated fractions containing oligomers showed a distinct absorption band at 840 nm that was not observed in the original Au_{25} monomer. It was also shown that this band disappeared to give a band at 690 nm characteristic of the Au_{25} monomer when the dithiol-bridged oligomers were treated with monothiol. Therefore, the newly appeared absorption band at 840 nm, observed in the fast-moving oligomer species, suggests electronic communication between the Au_{25} cores via *p*-conjugated aromatic linkers. Construction of such multi-cluster systems combined with *p*-conjugated bridges is interesting but still in its early stages. Further research to reveal the mechanism and optimize the synthesis protocol is expected.

Until now, the only high-dimensional GCAM with an X-ray single crystal structure was reported by the Wang group in 2014 [52]. Firstly, by using (2-(3-methylpyrazinyl)-diphenylphosphine) (mdppz) as protecting ligands, they prepared a cluster $[(C)(Au\text{-}mdppz)_6](BF_4)_2$, which bears six outward N donors that are available for coordination with metal ions in order to generate high-dimensional cluster-based polymers or frameworks (Figure 1.11a,b). Thus, the Au_6 cluster can be seen as a metal cluster linker. The cluster linker connects silver(I) ions with the outward N donors of its pyrazinyl groups to form a luminescent cluster-based MOF, $[(C)(Au\text{-}mdppz)_6Ag_6](BF_4)_8$, with twofold interpenetrated NbO topology, and hexagonal channels with a size of about 1.1 nm along the *c* axis (Figure 1.11c,d). Of note, although there are six outward N donors for extending connections, the Au_6 cluster only functions as a four-connected linker because of the terminal blocking of the silver ions by the H_2O molecules and BF_4^- counterions. The channels were available for solvent-molecule exchanges along with corresponding luminescence responses.

Of note, the assembly strategy through coordination has been employed by the Hyeon group. In 2021, they reported a highly fluorescent gold cluster assembly (GCA) with a QY of ~90%, which is synthesized by introducing Zn^{2+} ions to non-emissive $Au_4(SRCOO^-)_4$ clusters, by limiting the growth of gold precursor to oligomeric gold–thiolate ($(Au^I\text{–}SR)_x$) complex (Figure 1.12) [53]. Briefly, monomeric

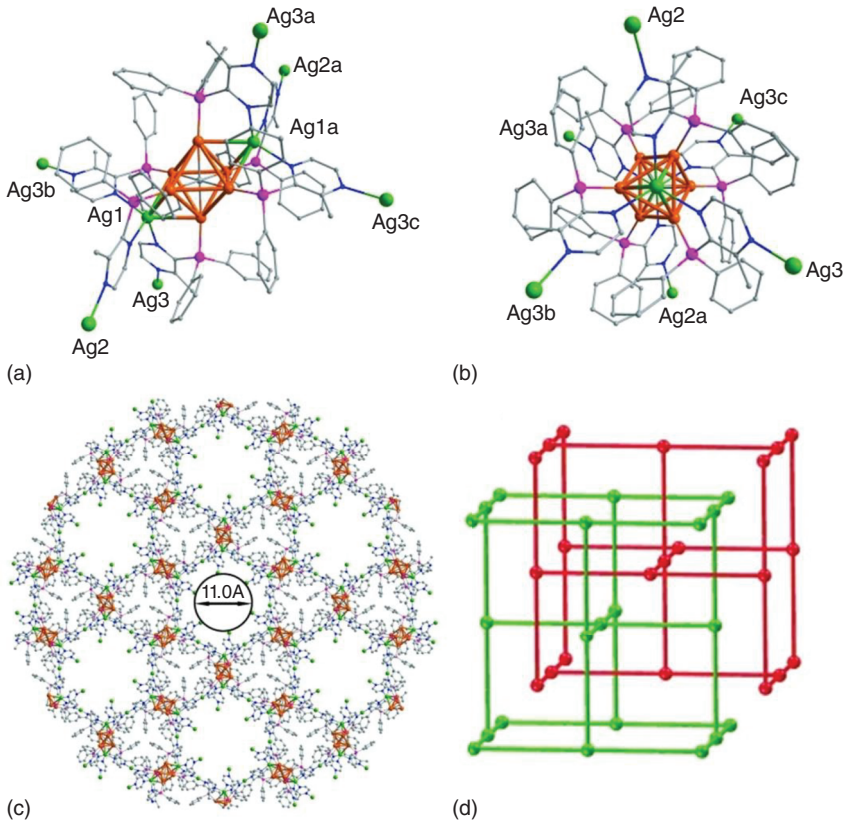

Figure 1.11 (a, b) Crystal structure of the C-$Au_6Ag_6(mdppz)_6$ nano-building block in different views. (c) Perspective view of Au_6Ag_6 cluster-based MOFs along the [0 0 1] direction. (d) Schematic illustration of the NbO topology in the twofold interpenetrated Au_6Ag_6 cluster-based MOFs. Colors: orange sphere, Au; green sphere, Ag; purple sphere, P; gray sphere, C; blue sphere, N. Source: Reproduced with permission from Ref. [52]. © 2014 John Wiley & Sons.

$Au_4(MHA)_4$ cluster was synthesized in an aqueous medium by adding excess mercaptohexanoate (MHA, S-$(CH_2)_5COO^-$) ligand to $HAuCl_4{\cdot}3H_2O$ solution. Then, Zn^{2+} ion is introduced to induce the assembly between monomeric $Au_4(MHA)_4$ clusters without changing the original structure of the gold cluster. The mercaptohexanoic acid (MHA–H) acts as a protecting ligand as well as a mild reductant that reduces Au(III) to Au(I). The formation of GCA is induced by introducing metal ions into the solution of $Au_4(MHA)_4$ cluster because metal ions can guide the formation of the superstructure from monomeric building blocks. The $Au_4(MHA)_4$ clusters are successfully assembled by the interaction between the anionic carboxylate group in the MHA ligand and Zn^{2+} ion in a cross-linking fashion.

The authors showed that unique aurophilic interaction between Au_4 clusters is responsible for the radiative channel that is unprecedented for conventional gold NCs and nanoparticles. And the rigidified chemical environment, which was

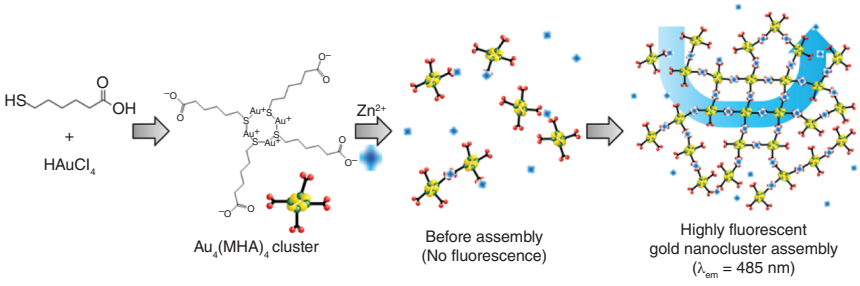

Figure 1.12 Synthesis of GCA. Source: With permission from Ref. [53]. © 2021 American Chemistry Society.

induced by the coordination of Zn^{2+} ion with the carboxylate group in the ligand, to delay vibrational relaxation accounts for the bright greenish-blue fluorescence.

Recently, the Yam group constructed an unprecedented gold(I) cluster cage $[Au_{24}\text{-}Cl]_C$ with $[(\mu_3\text{-}S)Au_3]^+$ units as the nodes or vertices and V-shaped 1,3-bis (diphenylphosphino)benzene ligand with 2-phenyl substituent as the organic building block [54]. The complex cation of $[Au_{24}\text{-}Cl]_C$ displays a cubic structure, where eight $[(\mu_3\text{-}S)Au_3]^+$ units occupy the vertices with the 12 diphosphine ligands spanning the edges of the cube. By virtue of the dynamic and reversible nature of the coordination bonds and aurophilic interactions, the gold(I) cluster cages exhibit interesting stimuli-responsive properties. A change of the counterions from Cl^- to PF_6^- or BF_4^- resulted in a structural transformation from a cubic structure of $[Au_{24}\text{-}PF_6]_C$ and $[Au_{24}\text{-}BF_4]_C$ to a rhombic prism structure of $[Au_{24}\text{-}PF_6]_{RP}$ and $[Au_{24}\text{-}BF_4]_{RP}$ during the crystallization process, which could be recovered upon dissolution. The complex cations of $[Au_{24}\text{-}PF_6]_{RP}$ and $[Au_{24}\text{-}BF_4]_{RP}$ display rhombic prism structures with two rhomboidal and four square faces, and the bidentate phosphine ligands occupy the 12 edges and are linked by eight $[(\mu_3\text{-}S)Au_3]^+$ vertices. Furthermore, upon heating the CD_3CN solution of $[Au_{24}\text{-}PF_6]_C$ at 353 K for around 0.5 hour, $[Au_{18}\text{-}PF_6]_{TP}$ was afforded, which displayed a triangular prism structure with six $[(\mu_3\text{-}S)Au_3]^+$ units occupying the vertices and nine ligands spanning the edges (Figure 1.13). The reverse transformation from $[Au_{18}\text{-}PF_6]_{TP}$ to $[Au_{24}\text{-}PF_6]_C$ could be realized in DMSO-d_6, CD_3CN, and acetone-d_6 solutions at room temperature. This work suggests a new perspective to construct GCAMs by predesigning the ligands and cluster nodes with the desired geometry and configuration.

1.4 Applications

Directional modification and functionalization of gold NCs through surface engineering could expand the potential applications of this kind of materials. On the other hand, besides the inherent properties of the individual metal clusters, the aggregation form of the gold NCs in GCAMs usually facilitates novel light, electricity, and magnetic behaviors that benefit from the unobstructed intercluster electronic communication.

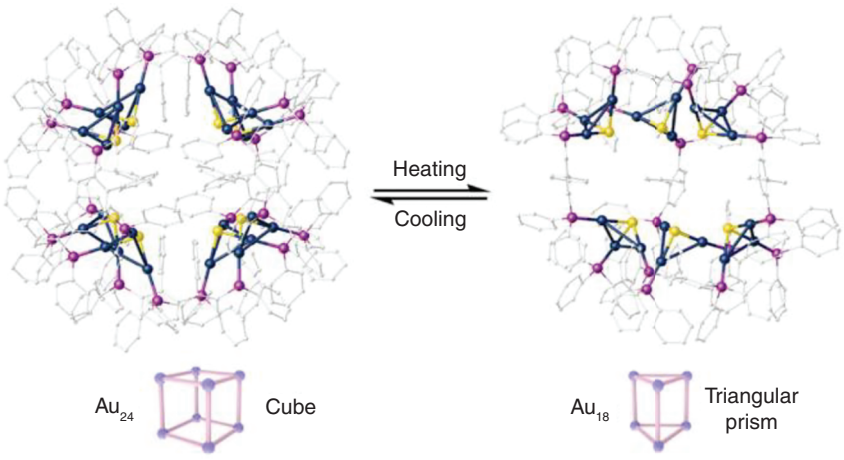

Figure 1.13 The structure transformation between the cubic Au_{24} cage and the triangular prism Au_{18} cage. Source: With permission from Ref. [54]. © 2021 American Chemical Society.

1.4.1 Biomedical Application

The GCA based on Au_4 clusters and Zn^{2+} can be disassembled and reassembled by the extraction and readdition of metal ions with the original structure of the Au_4 cluster maintained during the disassembly process [53]. Both the controllability of the dis/reassembly process and their structural similarity to metal–organic frameworks enable GCA to be applied as a biodegradable drug delivery system (DDS) that can be monitored by the distinct PL during its degradation and drug release. The representative anticancer drug, doxorubicin, was loaded into GCA to demonstrate its potential use as a trackable drug delivery vehicle. The hydrophobic doxorubicin can be successfully loaded inside GCA without changing the characteristic emission wavelength of GCA (Figure 1.14a). Gradual disassembly and drug release of drug-loaded GCA were confirmed by the decrease of PL and the increase of released drug in the solution (Figure 1.14a,b). Interestingly, the rate of drug release can be controlled by the rate of disassembly. The release rate of doxorubicin increases after 20 hours from the addition of the EDTA solution to the drug-loaded GCA. Cell viability analysis also confirms both the biocompatibility of GCA and its capability as a drug delivery vehicle, presenting efficient drug loading and release and sustaining the anticancer effect of doxorubicin (Figure 1.14c). Finally, cell imaging by confocal fluorescence microscopy was conducted to evaluate the performance of doxorubicin-loaded GCA as the trackable and self-indicating DDS (Figure 1.14d,e). Time-dependent confocal microscopy shows the gradual release of doxorubicin in the HeLa cell (Figure 1.14d,e, red) simultaneously with the dimming fluorescence of GCA (Figure 1.14d,e, blue). These unique features of strong fluorescence, with narrow wavelength following the degradation/disassembly status of the vehicle and release of the drug cargo, confirm the great potential of GCA as a trackable and degradable material, expanding theragnostic drug delivery in the future.

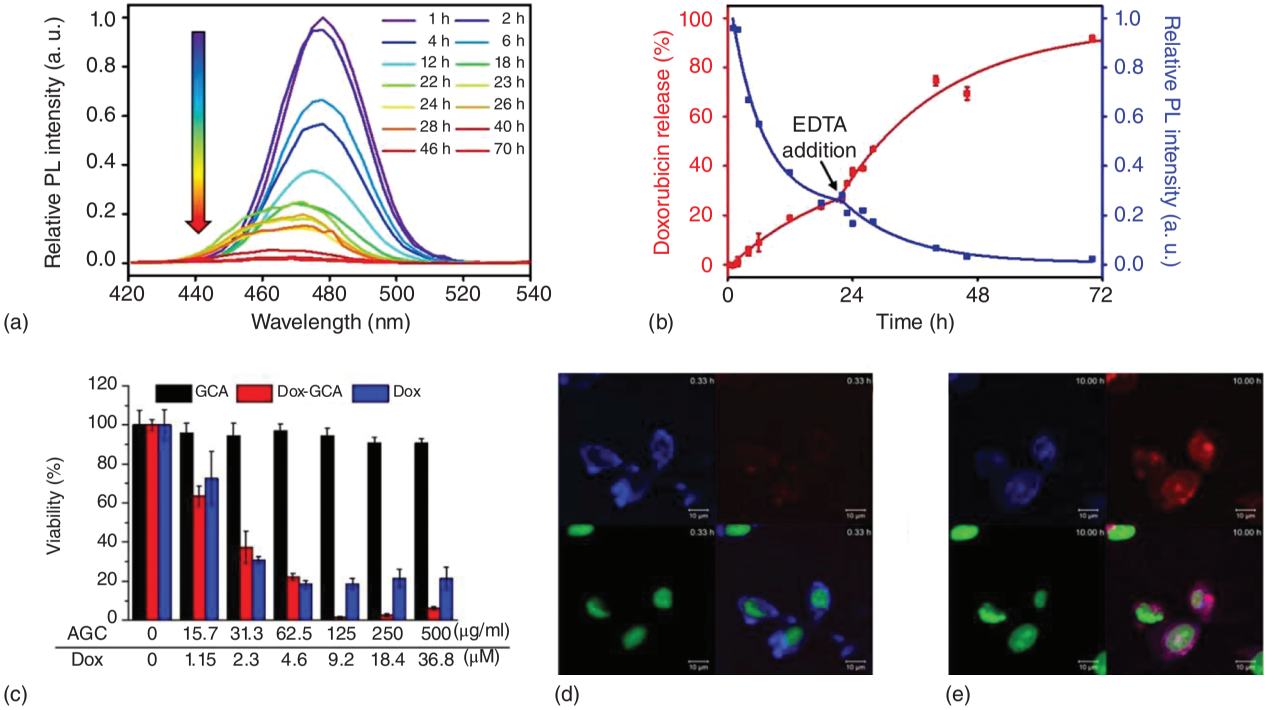

Figure 1.14 (a) Time-dependent change of PL spectrum of doxorubicin-loaded GCAs. (b) Release profiles of doxorubicin from Dox-GCA, and the PL intensity of GCA during release. EDTA was added at 22 hours to boost the release rate. (c) Evaluation of biocompatibility of GCA and anticancer effect of Dox-GCAs compared with free doxorubicin. (d, e) Confocal microscopy images of HeLa cells after the treatment of drug-loaded GCAs. 20 minutes after (d) and 10 hours after the treatment. Each color notes the emission from GCAs (blue), doxorubicin (red), and Draq5 (green, nucleus-staining). Source: Reproduced with permission from Ref. [53]. © 2021 American Chemistry Society.

1.4.2 Semiconductivity

$(AuAg)_{34n}$ comprises polymeric chains parallel to the *c*-axis of the single crystal, and these chains with direct metal–metal bonds connecting the clusters are separated in *a*- and *b*-directions by the bulky A-Adm ligands. This structural anisotropy promises a highly anisotropic (semi)conductivity. To prove this, FET devices were fabricated to measure the direction-dependent conductivity of the polymer crystals (Figure 1.15a). All the field-effect transistors showed an anisotropy of electrical conductivity (Figure 1.15b). The averaged electrical conductivity along the *c*-crystallographic axis of the crystal at room temperature and relative humidity of 56% is $1.49 \times 10^{-5}\,S\,m^{-1}$, which is 1800 times the electrical conductivity along the *a*-crystallographic axis.

The semiconductor properties of a single crystal along the *c*-crystallographic axis were studied with the transfer and output characteristic curves (Figure 1.15c,d).

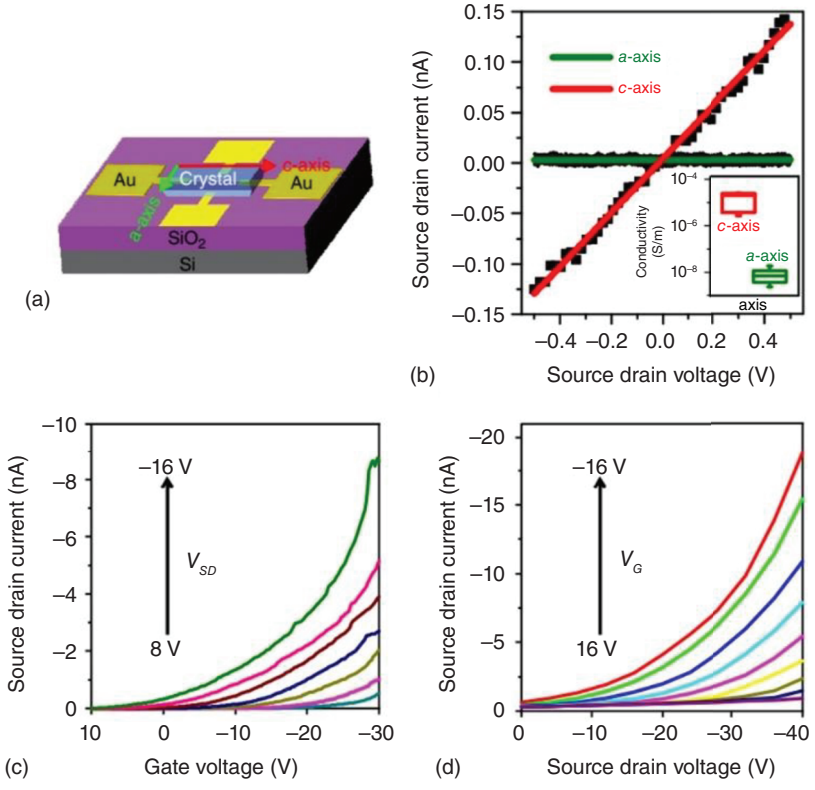

Figure 1.15 Electrical transport properties of the cluster polymer crystals. (a) The structure of the polymer crystal FET. (b) I–V plot of the polymer crystal along the *a*-axis and *c*-axis, respectively, with the range of corresponding conductivity values shown in the inset. (c) Transistor transfer (VSD = 8 to −16 V in −4 V steps), and (d) output characteristics (VG = 16 to −16 V in −4 V steps) measured along the *c*-axis of the polymer crystal. Channel length, width = 80, 50 μm. Source: With permission from Ref. [47]. © 2019 Springer Nature Limited.

The transfer curves show that at negative gate voltage (V_G), the source-drain currents increase with more negative V_G, demonstrating the p-type field effect. This indicates a hole conduction mechanism. The ON/OFF current ratio is around 4000, and the charge carrier mobility reaches 2.46×10^{-2} cm^2 V^{-1} s^{-1} at source-drain voltage (V_{SD}) = −16 V. The exponential behavior in the output curves is attributed to the Schottky barrier between the electrode and the polymer crystal. As a comparison, the reported photoconductive two-dimensional (2D) films of phosphine-thiolate-stabilized Au25 clusters [55], showed an ON/OFF ratio of about 50 000 for VSD = 6 V, charge carrier mobility approaching 10^{-5} cm^2 V^{-1} s^{-1} at VSD = 20 V, and n-type field effect. The mobility of the polymeric crystal $(AuAg)_{34n}$ is in the range of traditional *p*-type single-crystal organic semiconductors and close to the mobility of supercrystal of CdSe quantum dots [56–58]. The conductivity (1.49×10^{-5} S m^{-1}) of $(AuAu)_{34n}$ crystals in the *c*-crystallographic axis is one to three orders of magnitude higher than the values reported for thiolate-stabilized 1D assemblies of Au_{21} clusters where 1D "nanofibrils" of the clusters were formed by modulating the weak interactions between the ligand layers of the clusters [59]. These comparisons indicate that the conductivity and charge carrier mobility are increased by several orders of magnitude in the macroscopic cluster-based materials via direct linking of the clusters by the –Ag–Au–Ag– chains in the cluster polymer crystal.

1.4.3 Magnetism

$Au_{25}(SBu)_{18}^0$ is a paramagnetic monolayer-protected cluster that, in solution, displays the same molecule-like behavior of other Au_{25} clusters. In the solid state, however, a linear polymer $[Au_{25}(SBu)_{18}^0]_n$ composed of $Au_{25}(SBu)_{18}^0$ units interconnected by single Au—Au bonds is formed. The otherwise unpaired electrons of the $Au_{25}(SBu)_{18}^0$ clusters pair up, with the generation of a nonmagnetic ground state [46].

To explain this magnetic behavior, the authors conducted DFT calculations and compared the relative energies of the magnetic state and the nonmagnetic state of $[Au_{25}(SBu)_{18}^0]_n$. They found that in the crystal, the cluster has a nonmagnetic ground state that is lower in energy than the magnetic state by 27 meV. A nonmagnetic ground state implies that the otherwise unpaired electron in the isolated $Au_{25}(SBu)_{18}^0$ cluster is paired up in the ground state of the $Au_{25}(SBu)_{18}^0$ crystal, leading to a fully occupied valence band (VB) and an empty conduction band (CB). Further studies indicated that the energetics of nonmagnetic versus magnetic states are closely related to the intercluster distance or the closest Au–Au contact. When there is no close contact between two neighboring Au_{25} clusters, the magnetic state is preferred. On the other hand, when close contact occurs, the nonmagnetic state can be lower in energy than the magnetic state. The conclusion was supported by the reference research on two known clusters, $Au_{25}(SEt)_{18}^0$ and $Au_{25}(SC_2H_4Ph)_{18}^0$.

The authors also studied the cw-EPR behavior of the $[Au_{25}(SBu)_{18}^0]_n$ crystals in comparison with the spectrum obtained for a glassy toluene solution. The very different line width and the absence of a fine structure at 3000–4000 G for polymer $[Au_{25}(SBu)_{18}^0]_n$ show that the physical state in which $Au_{25}(SBu)_{18}^0$ is studied markedly affects the EPR signal. More specifically, the clusters in frozen solution display

the spectrum of distribution of randomly oriented $S = 1/2$ spin-state molecules with anisotropic g-tensor components. The temperature-dependent cw-EPR spectra of $[Au_{25}(SBu)_{18}^{0}]_n$ crystals and the estimated coupling energy (J) with the Hall expression revealed the fact that the double integrated EPR signal is an increasing function of T, indicating that thermal activation makes a higher energy magnetic state more populated, thereby confirming the DFT prediction that the ground state of $[Au_{25}(SBu)_{18}^{0}]_n$ is nonmagnetic. The best fit to the experimental data yields a J value of 28(2) meV, i.e. virtually identical to the DFT-calculated value of 27 meV. This outstanding agreement between EPR results and calculations thus provides compelling evidence that the $Au_{25}(SBu)_{18}^{0}$ clusters self-organize into a linear $S = 1/2$ antiferromagnetic polymer chain.

1.5 Conclusion

This chapter summarizes the surface engineering and hierarchical assembly of gold NCs with atom-precise composition and molecular structures. The surface modification of gold NCs is sorted out in detail according to different strategies, while the GCAMs are categorized by types of intercluster interactions. We gave an outline of the crystal structures of some typical examples and analyzed the opportunities and challenges. Benefiting from the novel structure features of the individual/aggregated metal cluster nodes, GCAMs show potential applications in many fields, including biomedicine, semiconductivity, and magnetism, to name a few. Several attractive representatives are introduced in the chapter.

In future work, new approaches to modify the ligand shell of gold NCs should be explored, which could conquer the shortcomings of gold NCs in specific applications. Controllable and designable GCAMs are desired in regard to the random assembly of hierarchical structures based on gold NCs. Also, the applications of gold-NC-based materials should be further pursued according to their functionality and advantages.

References

1 Chakraborty, I. and Pradeep, T. (2017). Atomically precise clusters of noble metals: emerging link between atoms and nanoparticles. *Chem. Rev.* 117: 8208–8271.
2 Jin, R., Zeng, C., Zhou, M., and Chen, Y. (2016). Atomically precise colloidal metal NCs and nanoparticles: fundamentals and opportunities. *Chem. Rev.* 116: 10346–10413.
3 Kang, X., Li, Y., Zhu, M., and Jin, R. (2020). Atomically precise alloy NCs: syntheses, structures, and properties. *Chem. Soc. Rev.* 49: 6443–6514.
4 Jin, Y., Zhang, C., Dong, X.-Y. et al. (2021). Shell engineering to achieve modification and assembly of atomically-precise silver clusters. *Chem. Soc. Rev.* 50: 2297–2319.

5 Chakraborty, P., Nag, A., Chakraborty, A., and Pradeep, T. (2019). Approaching materials with atomic precision using supramolecular cluster assemblies. *Acc. Chem. Res.* 52: 2–11.

6 Kang, X. and Zhu, M. (2019). Intra-cluster growth meets inter-cluster assembly: the molecular and supramolecular chemistry of atomically precise NCs. *Coordin. Chem. Rev.* 394: 1–38.

7 Zhang, M.-M., Li, K., and Zang, S.-Q. (2020). Progress in atomically precise coinage metal clusters with aggregation-induced emission and circularly polarized luminescence. *Adv. Opt. Mater.* 8: 1902152.

8 Goswami, N., Yao, Q., Luo, Z. et al. (2016). Luminescent metal NCs with aggregation-induced emission. *J. Phys. Chem. Lett.* 7: 962–975.

9 Rival, J.V., Mymoona, P., Lakshmi, K.M. et al. (2021). Self-assembly of precision noble metal NCs: hierarchical structural complexity, colloidal superstructures, and applications. *Small* 17: 2005718.

10 Luo, L. and Jin, R. (2021). Perspective atomically precise metal NCs meet metal-organic frameworks. *Iscience* 24: 103206.

11 Wang, Y. and Bürgi, T. (2021). Ligand exchange reactions on thiolate-protected gold NCs. *Nanoscale Adv.* 3: 2710–2727.

12 Dass, A., Stevenson, A., Dubay, G.R. et al. (2008). Nanoparticle MALDI-TOF mass spectrometry without fragmentation: $Au_{25}(SCH_2CH_2Ph)_{18}$ and mixed monolayer $Au_{25}(SCH_2CH_2Ph)_{18}$-x(L)x. *J. Am. Chem. Soc.* 130: 5940–5946.

13 Templeton, A.C., Wuelfing, W.P., and Murray, R.W. (2000). Monolayer protected cluster molecules. *Acc. Chem. Res.* 33: 27–36.

14 Guo, R., Song, Y., Wang, G.L., and Murray, R.W. (2005). Does core size matter in the kinetics of ligand exchanges of monolayer-protected au clusters? *J. Am. Chem. Soc.* 127: 2752–2757.

15 Shibu, E.S., Muhammed, M.A.H., Tsukuda, T., and Pradeep, T. (2008). Ligand exchange of $Au_{25}SG_{18}$ leading to functionalized gold clusters: spectroscopy, kinetics, and luminescence. *J. Phys. Chem. C* 112: 12168–12176.

16 Meng, X., Xu, Q., Wang, S., and Zhu, M. (2012). Ligand-exchange synthesis of selenophenolate-capped Au_{25} NCs. *Nanoscale* 4: 4161–4165.

17 Kurashige, W., Yamaguchi, M., Nobusada, K., and Negishi, Y. (2012). Ligand-induced stability of gold NCs: thiolate versus selenolate. *J. Phys. Chem. Lett.* 3: 2649–2652.

18 Zhong, J., Tang, X., Tang, J. et al. (2015). Density functional theory studies on structure, ligand exchange, and optical properties of ligand-protected gold NCs: thiolate versus selenolate. *J. Phys. Chem. C* 119: 9205–9214.

19 Niihori, Y., Matsuzaki, M., Pradeep, T., and Negishi, Y. (2013). Separation of precise compositions of noble metal clusters protected with mixed ligands. *J. Am. Chem. Soc.* 135: 4946–4949.

20 Heinecke, C.L., Ni, T.W., Malola, S. et al. (2012). Structural and theoretical basis for ligand exchange on thiolate monolayer protected gold NCs. *J. Am. Chem. Soc.* 134: 13316–13322.

21 Ni, T.W., Tofanelli, M.A., Phillips, B.D., and Ackerson, C.J. (2014). Structural basis for ligand exchange on $Au_{25}(SR)_{18}$. *Inorg. Chem.* 53: 6500–6502.

22 Yuan, X., Zhang, B., Luo, Z. et al. (2014). Balancing the rate of cluster growth and etching for GramScale synthesis of thiolate-protected Au_{25} NCs with atomic precision. *Angew. Chem. Int. Ed.* 53: 4623–4627.

23 Knoppe, S., Dharmaratne, A.C., Schreiner, E. et al. (2010). Ligand exchange reactions on Au_{38} and Au_{40} clusters: a combined circular dichroism and mass spectrometry study. *J. Am. Chem. Soc.* 132: 16783–16789.

24 Knoppe, S., Azoulay, R., Dass, A., and Bürgi, T. (2012). In situ reaction monitoring reveals a diastereoselective ligand exchange reaction between the intrinsically chiral $Au_{38}(SR)_{24}$ and chiral thiols. *J. Am. Chem. Soc.* 134: 20302–20305.

25 Wang, Y. and Bürgi, T. (2022). Evidence for stereoelectronic effects in ligand exchange reactions on Au_{25} NCs. *Nanoscale* 14: 2456–2464.

26 Suzuki, W., Takahata, R., Chiga, Y. et al. (2022). Control over ligand-exchange positions of thiolate-protected gold NCs using steric repulsion of protecting ligands. *J. Am. Chem. Soc.* 144: 12310–12320.

27 Lei, Z., Wan, X.-K., Yuan, S.-F. et al. (2018). Alkynyl approach toward the protection of metal NCs. *Acc. Chem. Res.* 51: 2465–2474.

28 Sugiuchi, M., Shichibu, Y., Nakanishi, T. et al. (2015). Cluster–π electronic interaction in a superatomic Au_{13} cluster bearing r-bonded acetylide ligands. *Chem. Commun.* 51: 13519–13522.

29 Hosier, C.A., Anderson, I.D., and Ackerson, C.J. (2020). Acetylide-for-thiolate and thiolate-for-acetylide exchange on gold NCs. *Nanoscale* 12: 6239–6242.

30 Narouz, M.R., Osten, K.M., Unsworth, P.J. et al. (2019). N-heterocyclic carbene-functionalized magic-number gold NCs. *Nat. Chem.* 11: 419–425.

31 Cao, Z., Gao, H., Qiu, M. et al. (2020). Chirality transfer from sub-nanometer biochemical molecules to sub-micrometer plasmonic metastructures: physiochemical mechanisms, biosensing, and bioimaging opportunities. *Adv. Mater.* 32: 1907151.

32 Yi, H., Osten, K.M., Levchenko, T.I. et al. (2021). Synthesis and enantioseparation of chiral Au_{13} nanoclusters protected by bis-N-heterocyclic carbene ligands. *Chem. Sci.* 12: 10436–10440.

33 Shen, H., Wu, Q., Malola, S. et al. (2022). N-heterocyclic carbene-stabilized gold nanoclusters with organometallic motifs for promoting catalysis. *J. Am. Chem. Soc.* 144: 10844–10853.

34 Luo, P., Bai, S., Wang, X. et al. (2021). Tuning the magic sizes and optical properties of atomically precise bidentate N-heterocyclic carbene-protected gold nanoclusters via subtle change of N-substituents. *Adv. Opt. Mater.* 9: 2001936.

35 Narouz, M.R., Takano, S., Lummis, P.A. et al. (2019). Robust, highly luminescent Au_{13} superatoms protected by N-heterocyclic carbenes. *J. Am. Chem. Soc.* 141: 14997–15002.

36 Kulkarni, V.K., Khiarak, B.N., Takano, S. et al. (2022). N-heterocyclic carbene-stabilized hydrido Au_{24} nanoclusters: synthesis, structure, and electrocatalytic reduction of CO_2. *J. Am. Chem. Soc.* 144: 9000–9006.

37 Lummis, P.A., Osten, K.M., Levchenko, T.I. et al. (2022). NHC-stabilized Au_{10} nanoclusters and their conversion to Au_{25} nanoclusters. *JACS Au* 2: 875–885.

38 Man, R.W.Y., Yi, H., Malola, S. et al. (2022). Synthesis and characterization of enantiopure chiral bis NHC-stabilized edge-shared Au10 nanocluster with unique prolate shape. *J. Am. Chem. Soc.* 144: 2056–2061.

39 Pei, X.-L., Zhao, P., Ube, H. et al. (2022). Asymmetric twisting of C-centered octahedral gold(I) clusters by chiral N-heterocyclic carbene ligation. *J. Am. Chem. Soc.* 144: 2156–2163.

40 Gabbaï, F.P., Schier, A., Riede, J., and Schmidbaur, H. (1997). Synthesis of the hexakis[(triphenylphosphane)gold(I)]methanium(2+) cation from trimethylsilyldiazomethane; crystal structure determination of the tetrafluoroborate salt. *Chem. Ber.* 130: 111–113.

41 Jia, J.-H. and Wang, Q.-M. (2009). Intensely luminescent gold(I)–silver(I) cluster with hypercoordinated carbon. *J. Am. Chem. Soc.* 131: 16634–16635.

42 Lei, Z., Pei, X.-L., Guan, Z.-J., and Wang, Q.-M. (2017). Full protection of intensely luminescent gold(I)–silver(I) cluster by phosphine ligands and inorganic anions. *Angew. Chem. Int. Ed.* 56: 7117–7120.

43 Gunawardene, P.N., Corrigan, J.F., and Workentin, M.S. (2019). Golden opportunity: a clickable azide-functionalized $[Au_{25}(SR)_{18}]-$ NC platform for interfacial surface modifications. *J. Am. Chem. Soc.* 141: 11781–11785.

44 Narita, K., Ishida, Y., Nukui, S. et al. (2021). Surface menshutkin S_N2 reaction on basic gold clusters provides novel opportunities for the cationization and functionalization of molecular metal clusters. *J. Phys. Chem. Lett.* 12: 11761–11765.

45 Saito, Y., Murata, C., Sugiuchi, M. et al. (2022). Ligand-coordinated metal clusters in condensed states: self-assemblies, crystals, and covalent networks. *Coordin. Chem. Rev.* 470: 214713.

46 De Nardi, M., Antonello, S., Jiang, D.E. et al. (2014). Gold nanowired: a linear $(Au_{25})_n$ polymer from Au_{25} molecular clusters. *ACS Nano* 8: 8505–8512.

47 Yuan, P., Zhang, R., Selenius, E. et al. (2020). Solvent-mediated assembly of atom-precise goldsilver NCs to semiconducting one-dimensional materials. *Nat. Commun.* 11: 2229.

48 Antonello, S., Dainese, T., Pan, F. et al. (2017). Electrocrystallization of monolayer-protected gold clusters: opening the door to quality, quantity, and new structures. *J. Am. Chem. Soc.* 139: 4168–4174.

49 Sokolowska, K., Hulkko, E., Lehtovaara, L., and Lahtinen, T. (2018). Dithiol-induced oligomerization of thiol-protected gold NCs. *J. Phys. Chem. C* 122: 12524–12533.

50 Jupally, V.R., Kota, R., Dornshuld, E.V. et al. (2011). Interstaple dithiol cross-linking in $Au_{25}(SR)_{18}$ nanomolecules: a combined mass spectrometric and computational study. *J. Am. Chem. Soc.* 133: 20258–20266.

51 Sels, A., Salassa, G., Cousin, F. et al. (2018). Covalently bonded multimers of $Au_{25}(SBut)_{18}$ as a conjugated system. *Nanoscale* 10: 12754–12762.

52 Lei, Z., Pei, X.-L., Jiang, Z.-G., and Wang, Q.-M. (2014). Cluster linker approach: preparation of a luminescent porous framework with NbO topology by linking silver ions with gold(I) clusters. *Angew. Chem. Int. Ed.* 53: 12771–12775.

53 Chang, H., Karan, N.S., Shin, K. et al. (2021). Highly fluorescent gold cluster assembly. *J. Am. Chem. Soc.* 143: 326–334.

54 Yan, L.-L., Yao, L.-Y., Ng, M., and Yam, V.W.-W. (2021). Stimuli-responsive and structure-adaptive three-dimensional gold(I) cluster cages constructed via "De-aurophilic" interaction strategy. *J. Am. Chem. Soc.* 143: 19008–19017.

55 Galchenko, M., Black, A., Heymann, L., and Klinke, C. (2019). Field effect and photoconduction in Au_{25} NCs films. *Adv. Mater.* 31: e1900684.

56 Jiang, H. and Hu, W. (2020). The emergence of organic single-crystal electronics. *Angew. Chem. Int. Ed.* 59: 1408–1428.

57 Chu, I.-H., Radulaski, M., Vukmirovic, N. et al. (2011). Charge transport in a quantum dot supercrystal. *J. Phys. Chem. C* 115: 21409–21415.

58 Talgorn, E., Abellon, R.D., Kooyman, P.J. et al. (2010). Supercrystals of CdSe quantum dots with high charge mobility and efficient electron transfer to TiO_2. *ACS Nano* 4: 1723–1731.

59 Li, Q., Russell, J.C., Luo, T.-Y. et al. (2018). Modulating the hierarchical fibrous assembly of au nanoparticles with atomic precision. *Nat. Commun.* 9: 3871.

60 Bonacchi, S., Antonello, S., Dainese, T., and Maran, F. (2021). Atomically precise metal NCs: novel building blocks for hierarchical structures. *Chem. Eur. J.* 27: 30–38.